processes

MDPI

Article

Research on Multi-Field Coupling Evolution Characteristics in Mature Thin Oil Fields During Energy-Storage Fracturing

Xiaolu Chen [1], Jianjun Zhang [1], Yingbiao Liu [1], Xiaochuan Tang [1], Zuxing Xiao [1], Zhenhu Lv [1] and Bo Wang [2,*]

[1] PetroChina Xinjiang Oilfield Company, Karamay 834000, China; chenxiaolu147@163.com (X.C.); 15033139254@163.com (J.Z.); lybpetro123@163.com (Y.L.); txcpetro123@163.com (X.T.); xiaozuxing130@163.com (Z.X.); lvzhswpu@163.com (Z.L.)
[2] China University of Petroleum-Beijing, Karamay 834000, China
* Correspondence: wangbo@cupk.edu.cn; Tel.: +86-180-9990-5217

Abstract

Mature thin oil reservoirs remain pivotal to maintaining reserves, sustaining production, and enhancing profitability due to their substantial annual output and untapped recovery potential. However, prolonged development leads to compromised fracturing efficacy, manifesting as severe formation-energy depletion, rapid production decline, and short effective periods of stimulation measures. Energy-storage fracturing technology addresses these challenges through fluid-injection energization and imbibition displacement, thereby replenishing formation energy and mobilizing residual oil. Leveraging a geo-engineering integrated platform, this study establishes an inverted seven-spot well-pattern energization model to systematically investigate pore pressure–stress field evolution and dynamic responses under varying energization parameters, including energy-storage injection rate, energy-storage volume, and energy-storage sequence. Key findings include: (1) increasing the energy-storage injection rate from 1.5 m^3/min to 3.5 m^3/min elevates average pore pressure by 7.8 MPa, with minimum and maximum horizontal principal stresses increasing by 1.4 MPa and 1.7 MPa, respectively; (2) raising the energy-storage volume from 2800 m^3 to 4200 m^3 enhances pore pressure by 5.5 MPa, accompanied by 2.5 MPa and 2.6 MPa increments in minimum and maximum horizontal principal stresses; (3) simultaneous energizing of all injection wells (1–6) is identified as the optimal injection sequence, yielding the highest average pore pressure of 40.3 MPa at equivalent monitoring positions within the well group, with corresponding average minimum and maximum horizontal principal stresses of 55.3 MPa and 60.3 MPa, respectively. The results provide theoretical and technical support for optimizing energy-storage fracturing strategies in mature thin oil reservoirs.

Keywords: mature thin oil reservoir; energy-storage fracturing; pore pressure–stress field; parameter optimization

Check for updates

Academic Editor: Dicho Stratiev

Received: 3 June 2026
Revised: 19 June 2026
Accepted: 29 June 2026
Published: 1 July 2026

Copyright: © 2026 by the authors. Licensee MDPI, Basel, Switzerland. This article is an open access article distributed under the terms and conditions of the Creative Commons Attribution (CC BY) license.

1. Introduction

Mature thin oil reservoirs exhibit high annual production and serve as a cornerstone for production stabilization and enhancement in the Xinjiang Oilfield. However, prolonged development has led to continuous formation pressure depletion, compromised fracturing efficiency, and widespread challenges, including inadequate fluid supply capacity and low-yield inefficiency in most production wells [1–7]. Urgent replenishment of formation energy is required to address imminent production maintenance pressures [8–11]. The group energy-storage fracturing technology, serving as a pivotal approach for stabilizing and

boosting production in mature reservoirs, demonstrates significant potential in elevating formation energy, enhancing imbibition-driven oil displacement, and unlocking residual oil reserves. This method improves intra-layer and inter-layer development efficiency, with preliminary field applications yielding tangible success.

Previous studies have demonstrated several application scenarios and technical advantages of energy-storage fracturing. Zheng Taiyi et al. [12] optimized CO_2 energy-storage huff-and-puff parameters for staged-fracturing horizontal wells in tight reservoirs, showing that gas injection can effectively supplement formation energy. Huang Ting et al. [13] proposed a process combining fracturing-fluid displacement injection and shut-in imbibition for ultra-low-permeability reservoirs, confirming that energy-storage fracturing can improve reservoir pressure and fracture-network complexity. He Haibin [14] developed fracture-network energy-enhancing fracturing through staged water injection, which increased dynamic imbibition efficiency and oil-water displacement efficiency in tight reservoirs. Zhang Hongni et al. [15] combined slickwater fracturing fluids with energy-storage fracturing in triple-low reservoirs to restore formation energy and improve stimulation effectiveness. Xiu Shuzhi et al. [16] further developed a low-damage energy-storage fracturing fluid system and integrated it with fracture-height control technology for low-permeability glutenite reservoirs. Overall, existing energy-storage fracturing technologies have mainly been applied to single-well huff-and-puff, fracturing-fluid system optimization, shut-in imbibition, and field process testing. These studies highlight the advantages of energy supplementation, enhanced imbibition displacement, improved fracture-network conductivity, and residual-oil mobilization. However, most previous work has focused on single wells or local treatment effects, while the pressure-conduction behavior, stress-superposition mechanism, and parameter-priority relationships under well-group energy-storage conditions remain insufficiently quantified.

Despite the effectiveness of energy-storage fracturing in field applications [13,17–21], the evolutionary characteristics of pore pressure–stress fields under well-group energy-storage conditions remain inadequately characterized in existing studies [22]. In particular, previous research has not fully clarified how injection rate, injected fluid volume, and injection sequence jointly control the spatial expansion of pore pressure and horizontal principal stress fields in an inverted seven-spot well pattern. Therefore, systematic numerical simulations are required to establish an optimization methodology for well-group energy-storage fracturing parameters. This study aims to quantify the multi-field coupling responses of a mature thin oil reservoir and provide theoretical and technical foundations for subsequent production-stabilization and enhancement strategies in mature oilfields.

Compared with previous studies that mainly addressed single-well huff-and-puff, fracturing-fluid systems, or field process tests, the present work focuses on the well-group scale of an inverted seven-spot pattern. The main distinction of this study is that pore pressure, minimum horizontal principal stress, and maximum horizontal principal stress are jointly evaluated under three engineering parameters, namely injection rate, energy-storage volume, and injection sequence. Therefore, this work provides a comparative framework for identifying parameter-priority relationships and well-group synergistic energization mechanisms rather than only describing single-well stimulation performance.

2. Model Establishment

2.1. Study Area Overview

Located in Jimsar County, the Bei-83 Well Block occupies the middle section of the piedmont structural belt. The block has an initial proven reserve of 1.08 million tons and an oil-bearing area of 1.7 km^2. The reservoir thickness ranges from 6 to 19 m, with an average effective thickness of 6.5 m. Development was initiated using an inverted

seven-spot well pattern with 300 m well spacing. The peak daily oil production reached 135 t/d, the cumulative oil production reached 217,000 t, and the recovery factor was 18.45%. With continuous production, the elastic energy of the reservoir was gradually depleted, the liquid-supply capacity of producing wells weakened, and the effective period of conventional stimulation became shorter. The reservoir deficit volume is estimated to be 33,000–44,000 m^3, and the designed energy-storage volume accounts for approximately 10% of this deficit volume. The reservoir is primarily driven by elastic expansion, with an original formation pressure of 38.47 MPa and a pressure coefficient of 1.45. The initial geostress field is characterized by a minimum horizontal principal stress of approximately 52 MPa in the geomechanical model, and the maximum horizontal principal stress is higher than the minimum horizontal stress, indicating a horizontal-stress-dominated stress regime. After long-term depletion, pressure drawdown around the well group caused a local reduction in pore pressure and strengthened the mismatch between formation energy and the original stress state. Petrophysical analysis reveals an average porosity of 21.05% and an average permeability of 6.82 mD, with strong heterogeneity. Lithologically, the reservoir comprises 73.5% lithic fragments, 18.4% feldspar, and minor quartz. Clay minerals are dominated by illite/smectite mixed-layer minerals (64.0%), followed by kaolinite (30.4%) and minor illite (5.6%), which impart moderate water sensitivity. These geological parameters, historical production data, and energy-deficit characteristics collectively indicate that the Bei-83 well group is suitable for evaluating well-group energy-storage fracturing.

2.2. Numerical Model and Coupling Method

Based on the geological characteristics of the inverted seven-spot well pattern in the Bei-83 well block, this study employs a multi-software collaborative modeling approach to conduct numerical hydraulic-fracturing simulations. Techlog software (v2020) was first used to standardize logging data and interpret reservoir parameters. The processed results were then imported into the Petrel numerical simulation platform to establish a three-dimensional geomechanical model, and an engineering-scale numerical fracturing model of the inverted seven-spot well pattern was constructed, as illustrated in Figure 1. A large-scale three-dimensional geological model (2010 m × 2010 m × 140 m) was built according to reservoir geomechanical properties to reduce boundary effects and ensure computational accuracy. The model was discretized using a structured hexahedral grid. Local grid refinement was adopted around injection wells, production wells, and the main fracture-propagation area, whereas the grid size was gradually enlarged toward the outer boundaries to balance computational efficiency and numerical accuracy. The hydraulic boundary was set as a closed boundary on the lateral and bottom surfaces, and rate-controlled injection was imposed at the injection wells. The geomechanical boundary conditions included fixed normal displacement on lateral boundaries, fixed vertical displacement at the bottom boundary, and overburden loading on the upper boundary. Initial pore pressure, minimum horizontal principal stress, and maximum horizontal principal stress were assigned according to logging interpretation and geomechanical inversion. The coupled seepage-stress problem was solved using an iterative poroelastic coupling procedure in which Darcy flow equations and geomechanical equilibrium equations were updated step by step. Dynamic time stepping was adopted to ensure convergence during high-rate injection. The principal parameters of the model include an average porosity of 21.05%, average permeability of 6.82 mD, pressure coefficient of 1.45, Young's modulus of 18 GPa, minimum horizontal principal stress of 52 MPa, and tensile strength of 4.2 MPa.

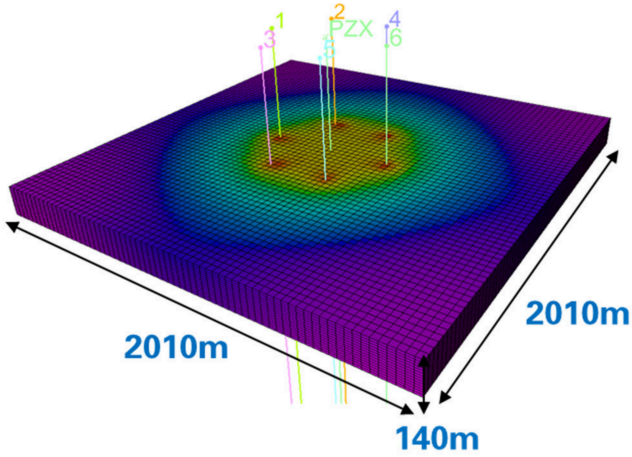


Figure 1. Inverted seven-spot hydraulic fracturing numerical model.

The governing seepage-stress coupling framework was further clarified. Fluid flow in the reservoir was described by mass conservation and Darcy flow [23,24], expressed as

$$\frac{\partial(\varphi\rho)}{\partial t} + \nabla \cdot (\rho v) = q \tag{1}$$

$$v = -\frac{k}{\mu}\nabla p \tag{2}$$

where φ is porosity, ρ is fluid density, v is Darcy velocity, k is permeability, μ is fluid viscosity, p is pore pressure, and q is the source/sink term.

The mechanical response was governed by the equilibrium equation [24,25]

$$\nabla \cdot \sigma + b = 0 \tag{3}$$

the effective-stress relationship being [24,25]

$$\sigma' = \sigma - \alpha p I \tag{4}$$

where σ is total stress, σ′ is effective stress, α is Biot coefficient, and I is the identity tensor.

The porosity, permeability, pressure coefficient, Young's modulus, in situ stresses, and tensile strength were assigned according to logging interpretation, petrophysical analysis, and geomechanical inversion of the Bei-83 well block. Constant-rate injection was applied in each simulation case, and the coupled pore-pressure and stress fields were updated iteratively at each time step until numerical convergence was achieved [26].

Model validation and field-data constraints were further clarified. The model was constrained by the original formation pressure (38.47 MPa), the recovery factor (18.45%), cumulative oil production (217,000 t), well spacing (300 m), and the estimated reservoir energy deficit (33,000–44,000 m^3). Because continuous downhole pressure monitoring and well-by-well flow-rate data were not available for every simulation case, the comparison with field performance is qualitative rather than a full history match. The simulated pressure-replenishment trend is consistent with the observed field requirement for energy supplementation after long-term production; nevertheless, quantitative validation against future pressure-gauge and production-dynamic data is still required. Based on the production data of individual wells during the initial stage of single-well flowback after energy storage, a production history fitting for individual wells was conducted (Figure 2). The results showed that the fitting effect exceeded 90%, further supporting the reliability of the model.

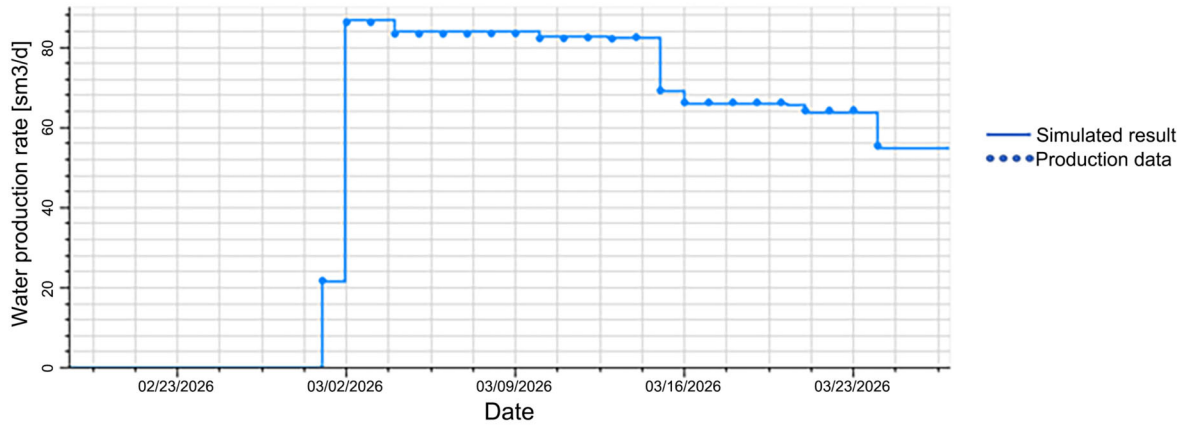


Figure 2. Fitting results of liquid extraction rate.

To improve repeatability, three monitoring grids for pressure and stress extraction were defined. The "equivalent monitoring positions" for extracting the average pore pressure and the horizontal principal stress were defined at the same relative positions in all simulation scenarios.

2.3. Simulation Schemes

Building upon the previously established numerical fracturing model of the inverted seven-spot well pattern, this study adopts the multi-factor orthogonal experimental design methodology to formulate 22 energy-storage simulation schemes. The work systematically investigates the evolutionary patterns and dynamic response characteristics of pore pressure–stress fields under varying energy-storage injection rates (1.5 to 3.5 m^3/min), energy-storage volumes (2800 to 4200 m^3), and different injection sequences. The detailed experimental design is shown in Table 1.

Table 1. Simulation schemes for well-group energy-storage fracturing.

Factors	Parameter Selection			
energy-storage volume (m^3)	2800 (A1)	3000 (A2)	3200 (A3)	3400 (A4)
energy-storage volume (m^3)	3600 (A5)	3800 (A6)	4000 (A7)	4200 (A8)
energy-storage injection rate (m^3/min)	1.5 (B1)	1.8 (B2)	2.0 (B3)	2.2 (B4)
energy-storage injection rate (m^3/min)	2.5 (B5)	2.8 (B6)	3.0 (B7)	3.5 (B8)
energy-storage sequence	sequential energizing (1-2-4-6-5-3)		sequential energizing (1-6-2-5-4-3)	
energy-storage sequence	sequential energizing (1-4-5-2-6-3)		simultaneous energizing (1~6)	
energy-storage sequence	sequential energizing (16-25-43)		sequential energizing (12-46-35)	

The injection-rate range of 1.5–3.5 m^3/min was selected according to the field pumping capacity, pressure-control requirements during stimulation, and operational safety margins for mature thin oil reservoirs. The energy-storage volume range of 2800–4200 m^3 was determined by combining the estimated reservoir energy deficit (33,000–44,000 m^3) with the field design principle that the injected energy-storage volume should account for approximately 10% of the deficit volume. Therefore, the lower limits represent conservative stimulation conditions, whereas the upper limits represent the maximum field-operational scale considered acceptable for avoiding excessive pressure build-up and uncontrolled fracture extension.

3. Analysis of Numerical Simulation Results

3.1. Energy-Storage Injection Rate

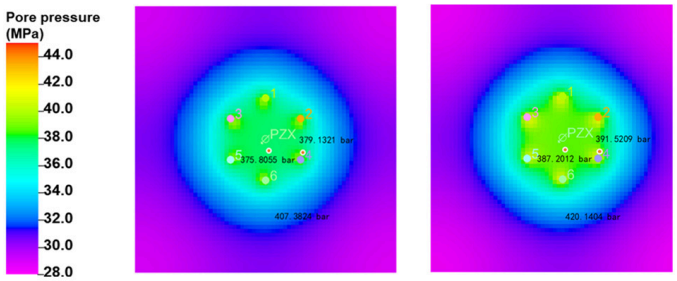
The inverted seven-spot well pattern model was configured with an energy-storage volume of 3600 m^3, employing simultaneous energization of injection wells (1~6) under constant-rate injection. Eight injection rate schemes (1.5 m^3/min, 1.8 m^3/min, 2.0 m^3/min, 2.2 m^3/min, 2.5 m^3/min, 2.8 m^3/min, 3.0 m^3/min, and 3.5 m^3/min) were implemented to systematically investigate pore pressure field evolution under varying energy-storage injection rates. As shown in Figure 3, the average pore pressures at identical monitoring locations measured 37.7 MPa, 38.9 MPa, 39.9 MPa, 40.5 MPa, 41.7 MPa, 42.8 MPa, 43.1 MPa, and 45.5 MPa respectively. The results demonstrate that the affected area of the pore pressure field exhibits a pronounced expansion trend with increasing injection rates. The peak pressure influence zone propagates from the immediate vicinity of the injection wells to encompass all regions within the inverted seven-spot well pattern configuration.

Figure 4 presents the pore pressure simulation results of the well group under varying energy-storage injection rates. Regression analysis of numerical simulation data reveals a correlation coefficient R = 0.99736 and coefficient of determination R^2 = 0.99473 between energy-storage injection rates and pore pressure, exhibiting a statistically significant linear positive correlation. As the injection rate increases from 1.5 m^3/min to 3.5 m^3/min, the average well-group pore pressure rises from 37.7 MPa to 45.5 MPa, yielding a net increase of 7.8 MPa (20.69% enhancement). Mechanistic analysis indicates that the energization medium influx velocity at higher injection rates exceeds the diffusion rate from fracture systems to matrix pores. This disequilibrium induces elevated fluid pressure within fractures, generating a steep fracture-matrix pressure gradient field. The resultant hydraulic potential drives imbibition-driven flow from fractures to matrix pores, thereby enhancing reservoir pore pressure.

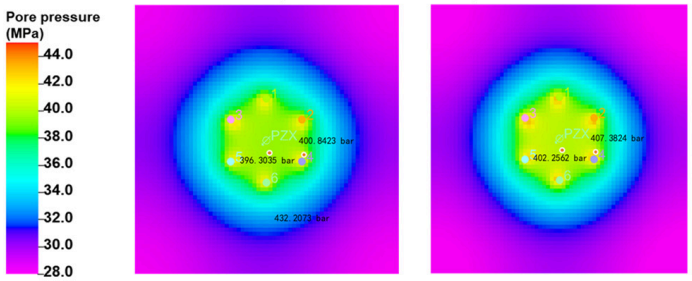
In Figure 4, the blue and red data points both represent numerical simulation results used for linear regression. The two colors are used only to distinguish different parameter-level groups visually, rather than to represent different data sources such as measured and simulated values. The fitted line indicates the overall linear relationship between the energy-storage injection rate and average pore pressure under the same model configuration.

Maintaining identical model configurations and energy-storage parameters (3600 m^3 volume, simultaneous energization of injection wells 1~6, constant-rate injection), this study investigates the evolutionary characteristics of well-group stress fields under controlled energy-storage injection rates (1.5~3.5 m^3/min) to reveal the coupling mechanism between injection rates and stress field dynamics. As shown in Figure 5, the average minimum horizontal principal stresses at equivalent monitoring positions measure 54.8 MPa, 55.0 MPa, 55.2 MPa, 55.3 MPa, 55.5 MPa, 55.7 MPa, 55.8 MPa, and 56.2 MPa, corresponding to injection rates of 1.5 m^3/min, 1.8 m^3/min, 2.0 m^3/min, 2.2 m^3/min, 2.5 m^3/min, 2.8 m^3/min, 3.0 m^3/min, and 3.5 m^3/min, respectively. The results demonstrate that the spatial propagation patterns of the minimum horizontal principal stress field exhibit charac-

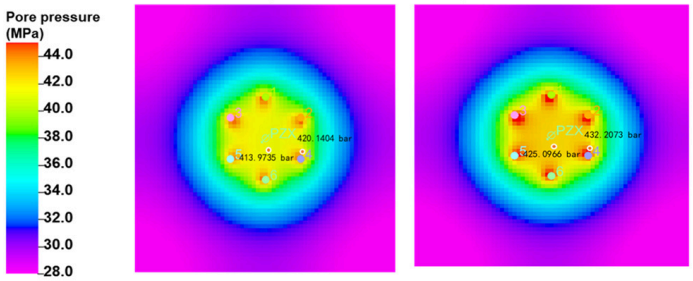
teristics analogous to those observed in pore pressure fields under identical energy-storage conditions. Increasing injection rates induce a significant expansion of the stress-affected zone. Notably, at 2.2 m^3/min, the peak stress influence transitions from localized regions near injection wells to fully saturate the inverted seven-spot well network.



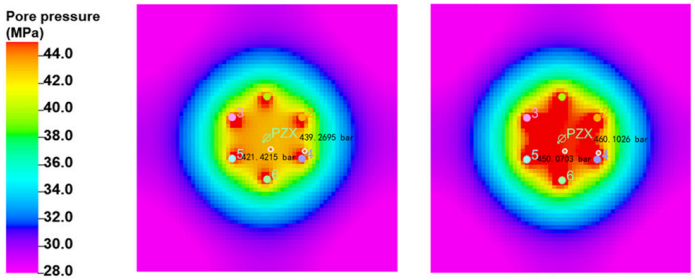
(a) The pore pressures with energy-storage injection rates of 1.5 m^3/min and 1.8 m^3/min



(b) The pore pressures with energy-storage injection rates of 2 m^3/min and 2.2 m^3/min



(c) The pore pressures with energy-storage injection rates of 2.5 m^3/min and 2.8 m^3/min



(d) The pore pressures with energy-storage injection rates of 3 m^3/min and 3.5 m^3/min

Figure 3. The pore pressure fields of the well group under different energy-storage injection rates. (**a**) The pore pressures with energy-storage injection rates of 1.5 m^3/min and 1.8 m^3/min; (**b**) The pore pressures with energy-storage injection rates of 2 m^3/min and 2.2 m^3/min; (**c**) The pore pressures with energy-storage injection rates of 2.5 m^3/min and 2.8 m^3/min; (**d**) The pore pressures with energy-storage injection rates of 3 m^3/min and 3.5 m^3/min.

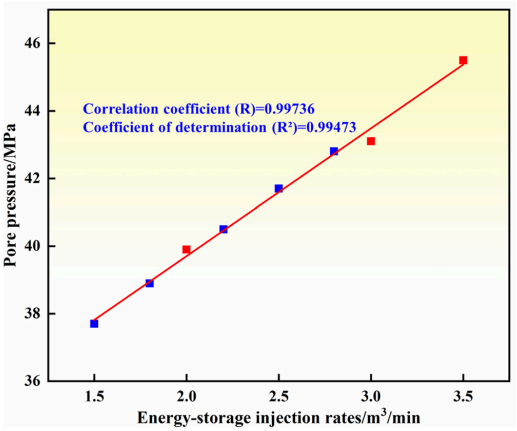
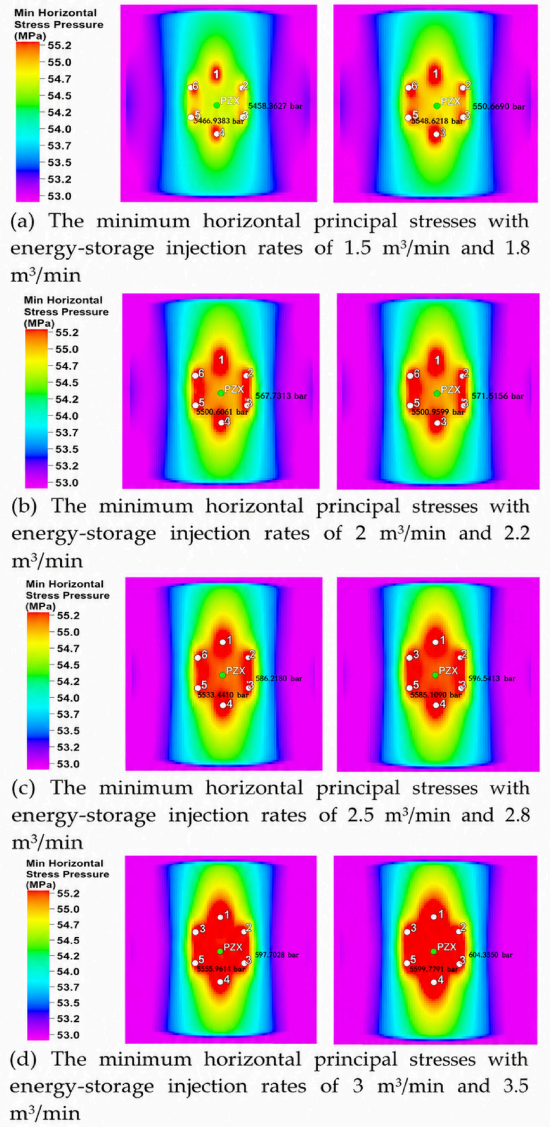


Figure 4. Simulation results of pore pressure in the well group under different energy-storage injection rates.



(a) The minimum horizontal principal stresses with energy-storage injection rates of 1.5 m³/min and 1.8 m³/min

(b) The minimum horizontal principal stresses with energy-storage injection rates of 2 m³/min and 2.2 m³/min

(c) The minimum horizontal principal stresses with energy-storage injection rates of 2.5 m³/min and 2.8 m³/min

(d) The minimum horizontal principal stresses with energy-storage injection rates of 3 m³/min and 3.5 m³/min

Figure 5. The well group's minimum horizontal principal stress fields under different energy-storage injection rates. (**a**) The minimum horizontal principal stresses with energy-storage injection rates of 1.5 m^3/min and 1.8 m^3/min; (**b**) The minimum horizontal principal stresses with energy-storage injection rates of 2 m^3/min and 2.2 m^3/min; (**c**) The minimum horizontal principal stresses with energy-storage injection rates of 2.5 m^3/min and 2.8 m^3/min; (**d**) The minimum horizontal principal stresses with energy-storage injection rates of 3 m^3/min and 3.5 m^3/min.

The simulated minimum horizontal principal stresses of the well group under varying energy-storage injection rates are presented in Figure 6. Linear regression analysis of the average minimum horizontal principal stress yields a correlation coefficient R = 0.99846 and a coefficient of determination R^2 = 0.99692, demonstrating a statistically significant linear positive correlation between injection rates and stress evolution. Increasing the injection rate from 1.5 m^3/min to 3.5 m^3/min elevates the minimum horizontal principal stress from 54.8 MPa to 56.2 MPa, corresponding to a net stress increase of 1.4 MPa (2.55% enhancement). Mechanistic quantification reveals a linear sensitivity coefficient of 0.7 MPa per 1 m^3/min increment in injection rate. Notably, the stress field exhibits significantly lower sensitivity to injection rate variations than the pore pressure field.

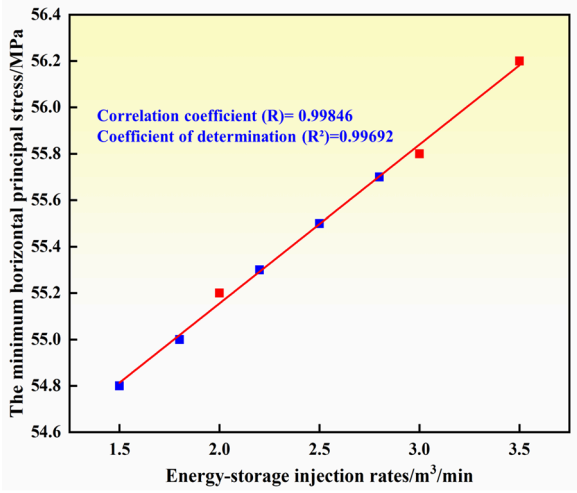
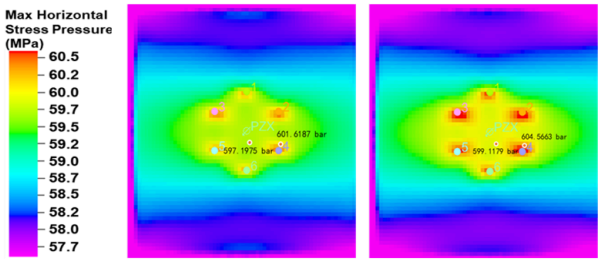


Figure 6. Simulation results of the minimum horizontal principal stresses in the well group under different energy-storage injection rates.

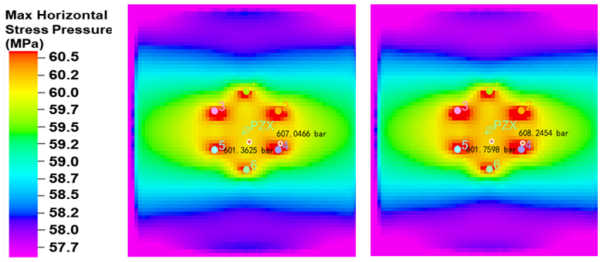
Under identical energy storage volume, energy-storage sequence, and constant-rate injection conditions, this study investigates the dynamic response characteristics of the injection rate versus the maximum horizontal principal stress field. Figure 7 illustrates the maximum horizontal principal stress variations in well groups under different energy-storage injection rates. When energy-storage injection rate increases progressively from 1.5 m^3/min, 1.8 m^3/min, 2.0 m^3/min, 2.2 m^3/min, 2.5 m^3/min, 2.8 m^3/min, 3.0 m^3/min, and 3.5 m^3/min, the average maximum horizontal principal stresses at equivalent locations within the well groups measure 59.9 MPa, 60.2 MPa, 60.4 MPa, 60.5 MPa, 60.8 MPa, 61 MPa, 61.2 MPa, and 61.6 MPa, respectively. Analysis reveals a pronounced synergistic effect between the disturbance range of the maximum horizontal principal stress field and the evolution patterns of the pore pressure field and the minimum horizontal principal stress field in the well groups. The affected area of the maximum horizontal principal stress field demonstrates significant expansion with increasing energy-storage injection rates. Notably, at an injection rate of 2.8 m^3/min, the peak influence range of the maximum horizontal principal stress extends from the vicinity of injection wells to encompass all regions within the inverted seven-spot well pattern.

The simulated maximum horizontal principal stresses of the well group under varying energy-storage injection rates are presented in Figure 8. Linear regression analysis of the average maximum horizontal principal stress yields a correlation coefficient R = 0.99884 and a coefficient of determination R^2 = 0.99748, indicating a statistically significant, linear, positive correlation between injection rates and stress evolution. When the energy-storage injection rate increases from 1.5 m^3/min to 3.5 m^3/min, the maximum horizontal principal stress rises from 59.9 MPa to 61.6 MPa, corresponding to a net increase of 1.7 MPa (2.83% enhancement). The stress sensitivity coefficient is quantified as 0.8 MPa per 1 m^3/min increment

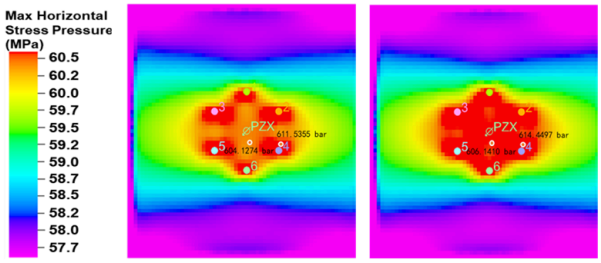
in injection rate. These results are closely aligned with the observed effects of energy-storage injection rates on the minimum horizontal principal stress field, demonstrating that the minimum and maximum horizontal principal stress fields respond synchronously to injection rate variations.



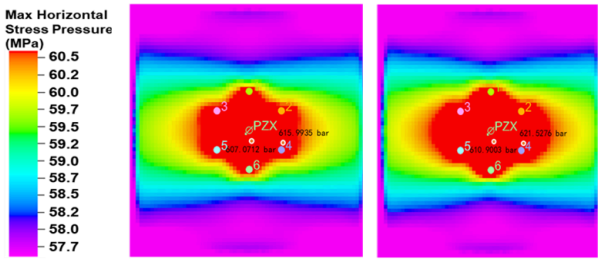
(a) The maximum horizontal principal stresses with energy-storage injection rates of 1.5 m³/min and 1.8 m³/min



(b) The maximum horizontal principal stresses with energy-storage injection rates of 2 m³/min and 2.2 m³/min



(c) The maximum horizontal principal stresses with energy-storage injection rates of 2.5 m³/min and 2.8 m³/min



(d) The maximum horizontal principal stresses with energy-storage injection rates of 3 m³/min and 3.5 m³/min

Figure 7. The well group's maximum horizontal principal stress fields under different energy-storage injection rates. (**a**) The maximum horizontal principal stresses with energy-storage injection rates of 1.5 m^3/min and 1.8 m^3/min; (**b**) The maximum horizontal principal stresses with energy-storage injection rates of 2 m^3/min and 2.2 m^3/min; (**c**) The maximum horizontal principal stresses with energy-storage injection rates of 2.5 m^3/min and 2.8 m^3/min; (**d**) The maximum horizontal principal stresses with energy-storage injection rates of 3 m^3/min and 3.5 m^3/min.

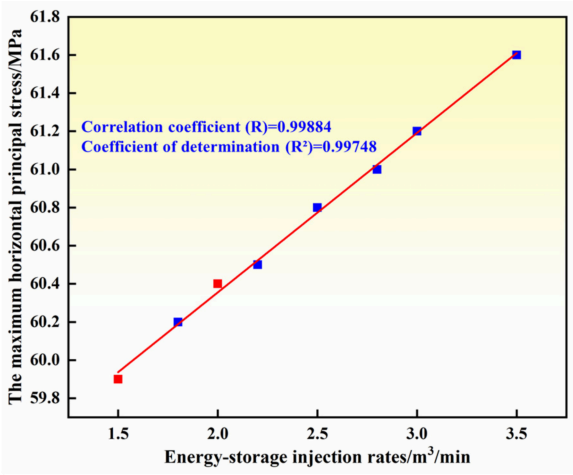


Figure 8. Simulation results of the maximum horizontal principal stresses in the well group under different energy-storage injection rates.

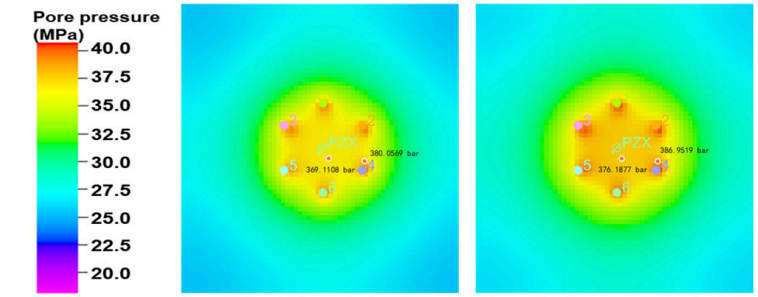
3.2. Energy-Storage Volume

With an energy-storage injection rate of 2 m^3/min and simultaneous energization of injection wells (1~6) under constant-rate injection, simulations were conducted at energy-storage volumes of 2800 m^3, 3000 m^3, 3200 m^3, 3400 m^3, 3600 m^3, 3800 m^3, 4000 m^3, and 4200 m^3. This study systematically investigates pore pressure field evolution under varying energy-storage volumes and utilizes the inverted seven-spot well pattern fracturing model. The pore pressures of the well group under varying energy-storage volumes are illustrated in Figure 9. The average pore pressures at equivalent monitoring positions measure 37.5 MPa, 38.2 MPa, 39.1 MPa, 39.7 MPa, 40.4 MPa, 41.3 MPa, 42.3 MPa, and 43.0 MPa, respectively. Increasing the energy-storage volume significantly expands the influence domain of the well group's pore pressure stress field. The peak pore pressure propagation evolves from localized regions near injection wells to fully saturate the entire internal area of the well network.

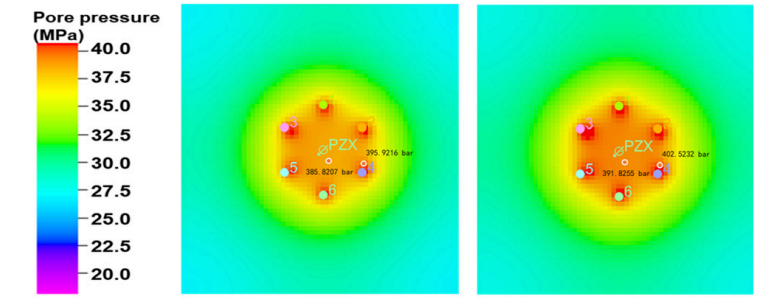
The simulated pore pressure results of the well group under varying energy-storage volumes are presented in Figure 10. Regression analysis of the numerical simulation data yields a correlation coefficient R = 0.9984 and a coefficient of determination R^2 = 0.9968, demonstrating a strong linear positive correlation between energy-storage volume and pore pressure. Increasing the energy-storage volume from 2800 m^3 to 4200 m^3 elevates the average well-group pore pressure from 37.5 MPa to 43.0 MPa, corresponding to a net increase of 5.5 MPa (14.67% enhancement). The pressure sensitivity coefficient is quantified as 0.8 MPa per 200 m^3 increment in energy-storage volume. Analytical results based on Biot's poroelastic theory demonstrate that reservoir pressure is jointly sustained by the rock matrix and pore fluids. With increasing injection volume of the energy-storage medium, the effective stress borne by the rock matrix is significantly reduced, leading to a marked enhancement in the reservoir's pore pressure.

Maintaining the aforementioned model configuration and energy-storage parameters, this study investigates the evolutionary characteristics of the well-group stress field under fine-tuned energy-storage volumes, systematically revealing the coupling mechanism between energy-storage volume and stress field dynamics. As shown in Figure 11, the average minimum horizontal principal stresses at equivalent monitoring positions measure 54.1 MPa, 54.4 MPa, 54.8 MPa, 55.2 MPa, 55.5 MPa, 55.9 MPa, 56.3 MPa, and 56.6 MPa, corresponding to energy-storage volumes of 2800 m^3, 3000 m^3, 3200 m^3, 3400 m^3, 3600 m^3, 3800 m^3, 4000 m^3, and 4200 m^3, respectively. The propagation patterns of the minimum horizontal principal stress field exhibit consistent trends with those observed in pore pressure field evolution. Increasing the energy-storage volume induces a significant expansion

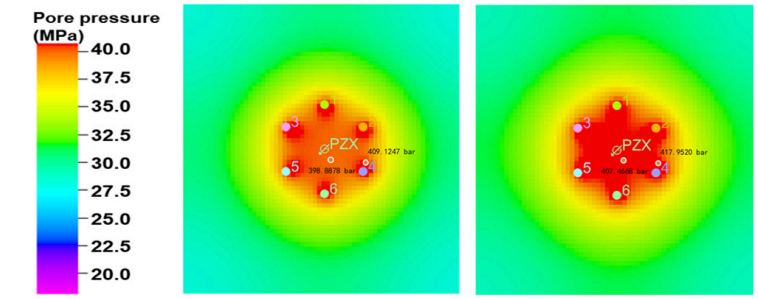
of the stress-affected domain, with the peak stress influence zone progressively extending from the vicinity of the injection wells to encompass the interior regions of the inverted seven-spot well pattern.



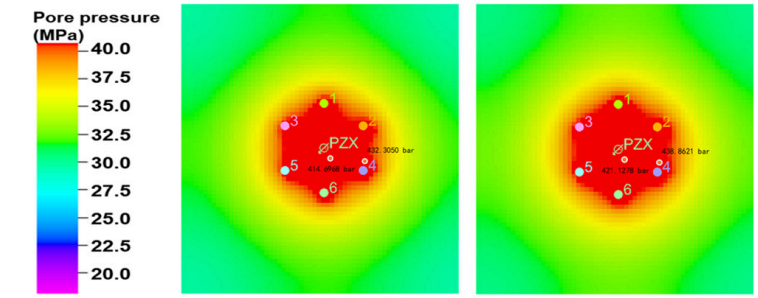
(a) The pore pressures with energy-storage volumes of 2800 m³ and 3000 m³



(b) The pore pressures with energy-storage volumes of 3200 m³ and 3400 m³



(c) The pore pressures with energy-storage volumes of 3600 m³ and 3800 m³



(d) The pore pressures with energy-storage volumes of 4000 m³ and 4200 m³

Figure 9. The pore pressure fields of the well group under different energy-storage volumes. (**a**) The pore pressures with energy-storage volumes of 2800 m^3 and 3000 m^3; (**b**) The pore pressures with energy-storage volumes of 3200 m^3 and 3400 m^3; (**c**) The pore pressures with energy-storage volumes of 3600 m^3 and 3800 m^3; (**d**) The pore pressures with energy-storage volumes of 4000 m^3 and 4200 m^3.

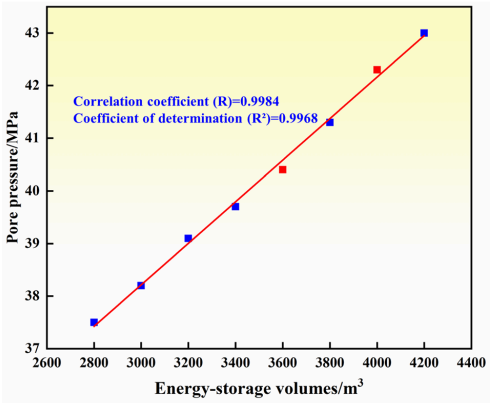
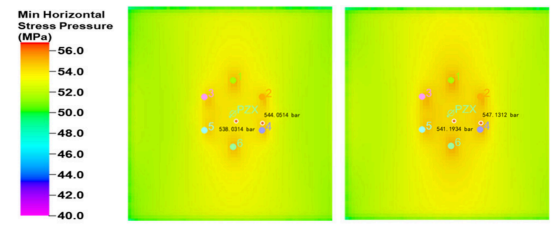
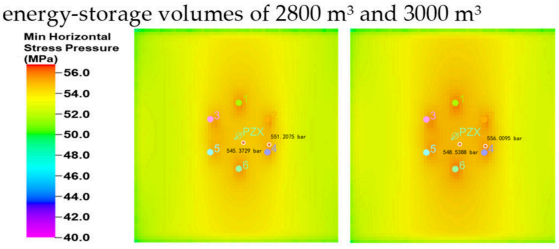


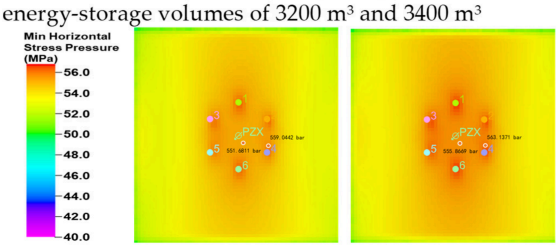
Figure 10. Simulation results of the pore pressure in the well group under different energy-storage volumes.



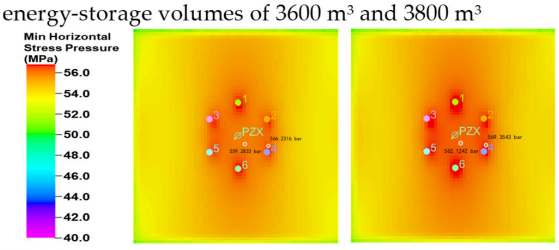
(a) The minimum horizontal principal stresses with energy-storage volumes of 2800 m³ and 3000 m³



(b) The minimum horizontal principal stresses with energy-storage volumes of 3200 m³ and 3400 m³



(c) The minimum horizontal principal stresses with energy-storage volumes of 3600 m³ and 3800 m³



(d) The minimum horizontal principal stresses with energy-storage volumes of 4000 m³ and 4200 m³

Figure 11. The minimum horizontal principal stress fields of the well group under different energy-storage volumes. (**a**) The minimum horizontal principal stresses with energy-storage volumes of 2800 m^3 and 3000 m^3; (**b**) The minimum horizontal principal stresses with energy-storage volumes of 3200 m^3 and 3400 m^3; (**c**) The minimum horizontal principal stresses with energy-storage volumes of 3600 m^3 and 3800 m^3; (**d**) The minimum horizontal principal stresses with energy-storage volumes of 4000 m^3 and 4200 m^3.

The simulated minimum horizontal principal stresses of the well group under varying energy-storage volumes are presented in Figure 12. Linear regression analysis of the average minimum horizontal principal stress yields a correlation coefficient R = 0.99942 and a coefficient of determination R^2 = 0.99885, demonstrating a statistically significant linear positive correlation between energy-storage volume and stress evolution. Increasing the energy-storage volume from 2800 m^3 to 4200 m^3 elevates the average minimum horizontal principal stress from 54.1 MPa to 56.6 MPa, corresponding to a net stress increase of 2.5 MPa (4.62% enhancement). The stress gradient sensitivity is quantified as 0.36 MPa per 200 m^3 increment in energy-storage volume. Notably, the minimum horizontal principal stress field exhibits lower sensitivity to energy-storage volume variations than the pore pressure field. This comparative analysis reveals analogous response characteristics between the pore pressure–minimum horizontal stress fields and the energy-storage volume, consistent with the previously observed coupling behavior under energy-storage injection rate variations.

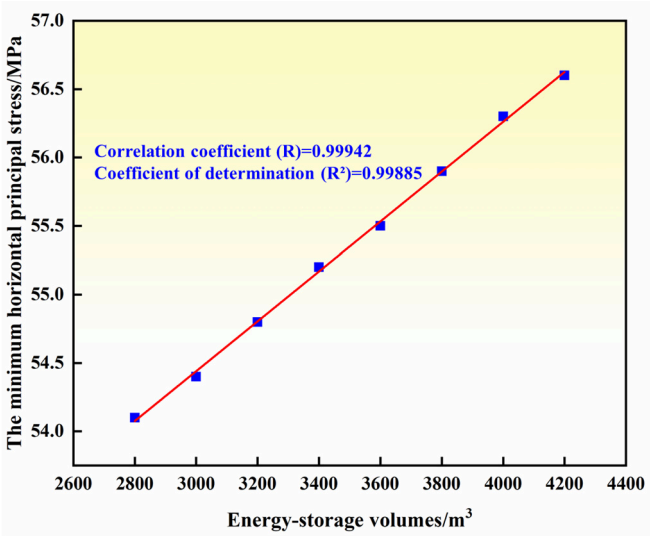
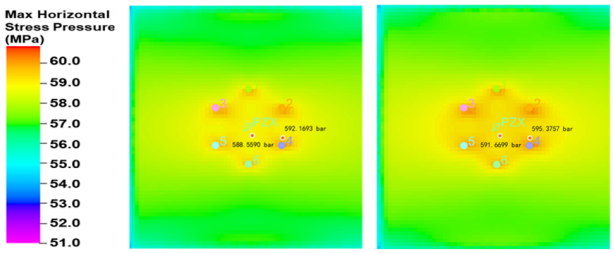


Figure 12. Simulation results of the minimum horizontal principal stresses in the well group under different energy-storage volumes.

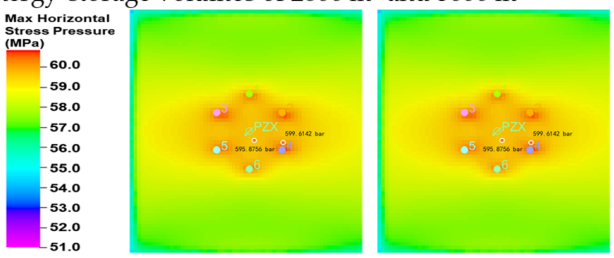
Under identical energy-storage volume, energy-storage sequence, and constant-rate injection conditions, this study further investigates the synergistic response mechanism of the maximum horizontal principal stress to energy-storage volume variations. The maximum horizontal principal stresses of the well group under varying energy-storage volumes are presented in Figure 13. The average maximum horizontal principal stresses at equivalent monitoring positions measure 59.0 MPa, 59.3 MPa, 59.8 MPa, 60.3 MPa, 60.6 MPa, 60.8 MPa, 61.3 MPa, and 61.6 MPa, corresponding to energy-storage volumes of 2800 m^3, 3000 m^3, 3200 m^3, 3400 m^3, 3600 m^3, 3800 m^3, 4000 m^3, and 4200 m^3, respectively. The results reveal that the propagation range of the maximum horizontal principal stress field significantly exceeds that of both the pore pressure field and the minimum horizontal principal stress field. As the energy-storage volume increases, the influence zone of the peak maximum horizontal principal stress progressively expands from localized areas near injection wells to fully encompass all internal regions of the inverted seven-spot well pattern.

The simulated maximum horizontal principal stresses of the well group under varying energy-storage volumes are presented in Figure 14. Regression analysis of the average maximum horizontal principal stress yields a correlation coefficient R = 0.99558 and a coefficient of determination R^2 = 0.99119, demonstrating a statistically significant linear positive correlation between energy-storage volume and stress evolution. Increasing the

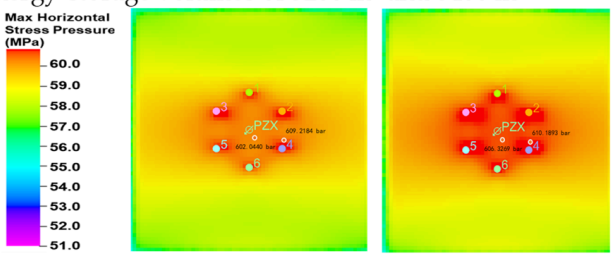
energy-storage volume from 2800 m^3 to 4200 m^3 elevates the maximum horizontal principal stress from 59.0 MPa to 61.6 MPa, corresponding to a net increase of 2.6 MPa (4.41% enhancement). The stress sensitivity coefficient is quantified as 0.36 MPa per 200 m^3 increment in energy-storage volume. Analytical results indicate that the response characteristics of the minimum and maximum horizontal principal stress fields to energy-storage volume variations are consistent with each other; however, both exhibit lower sensitivity compared to the pore pressure field.



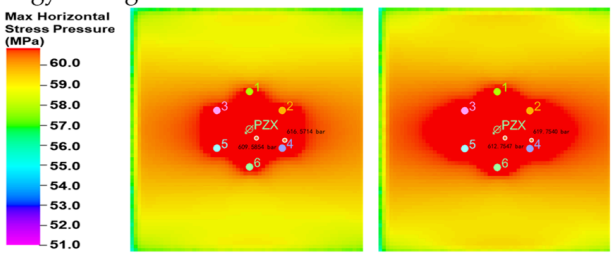
(a) The maximum horizontal principal stresses with energy-storage volumes of 2800 m^3 and 3000 m^3



(b) The maximum horizontal principal stresses with energy-storage volumes of 3200 m^3 and 3400 m^3



(c) The maximum horizontal principal stresses with energy-storage volumes of 3600 m^3 and 3800 m^3



(d) The maximum horizontal principal stresses with energy-storage volumes of 4000 m^3 and 4200 m^3

Figure 13. The maximum horizontal principal stress fields of the well group under different energy-storage volumes. (**a**) The maximum horizontal principal stresses with energy-storage volumes of 2800 m^3 and 3000 m^3; (**b**) The maximum horizontal principal stresses with energy-storage volumes of 3200 m^3 and 3400 m^3; (**c**) The maximum horizontal principal stresses with energy-storage volumes of 3600 m^3 and 3800 m^3; (**d**) The maximum horizontal principal stresses with energy-storage volumes of 4000 m^3 and 4200 m^3.

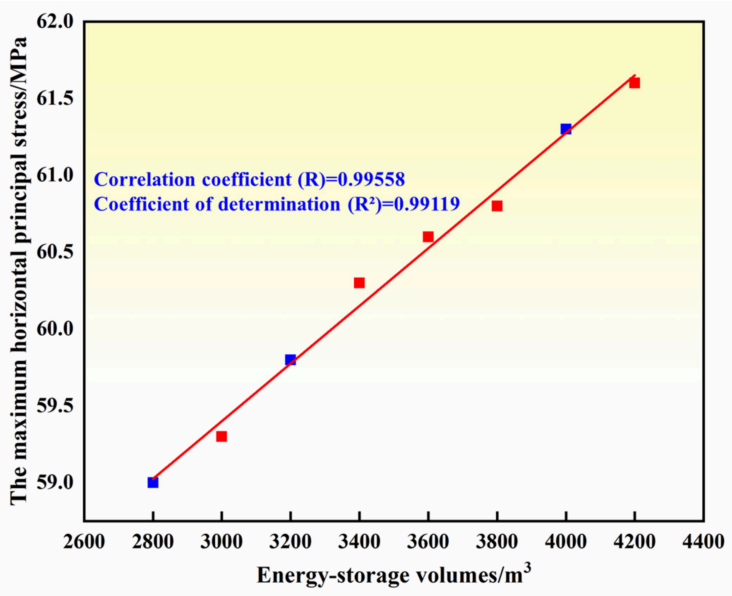
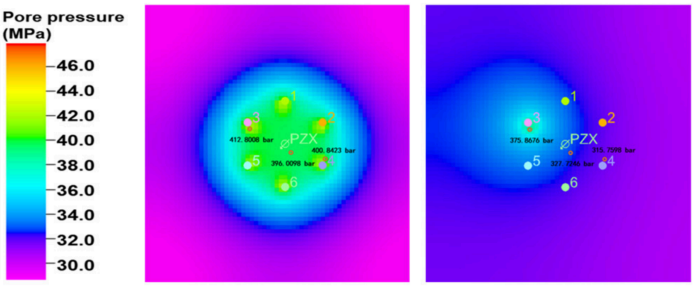


Figure 14. Simulation results of the maximum horizontal principal stresses in the well group under different energy-storage volumes.

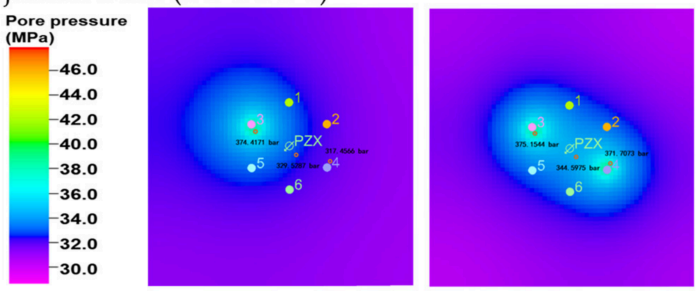
3.3. Energy-Storage Sequences

The inverted seven-spot well pattern model was configured with an energy-storage injection rate of 2 m^3/min and a total energy-storage volume of 3600 m^3. Using constant-rate injection, simulations were conducted using six distinct energization sequences: simultaneous energizing of injection wells (1~6), sequential energizing of injection wells (1-6-2-5-4-3), sequential energizing of injection wells (1-4-5-2-6-3), sequential energizing of injection wells (1-2-4-6-5-3), sequential energizing of injection wells (16-25-43), and sequential energizing of injection wells (12-46-53). As shown in Figure 15, the average pore pressures of the well group under sequential energizing sequences (1-2-4-6-5-3), (1-6-2-5-4-3), (1-4-5-2-6-3), (16-25-43), and (12-46-53) were 33.9 MPa, 34.1 MPa, 34.0 MPa, 36.4 MPa, and 35.1 MPa, respectively. In contrast, with simultaneous energization of injection wells (1~6), the average pore pressure at equivalent monitoring positions reached 40.3 MPa.

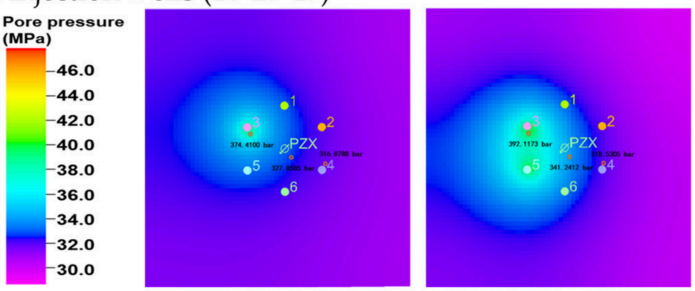
The analysis reveals distinct spatial distributions of pore pressure fields under different energization sequences. Under single-well sequential energization, the sequences (1-2-4-6-5-3), (1-6-2-5-4-3), and (1-4-5-2-6-3) yield similar pressure-field patterns, with average pore pressures of 33.9 MPa, 34.1 MPa, and 34.0 MPa, respectively. Because each well is energized at a different time, early-injected pressure has sufficient time to dissipate into the matrix and surrounding area before later wells begin injection; therefore, the pressure-conduction time effect weakens the final pressure accumulation in the well group. Under dual-well synchronized sequential energization, the average pore pressures increase to 36.4 MPa for (16-25-43) and 35.1 MPa for (12-46-53), indicating that simultaneous operation of two wells shortens the time lag between adjacent pressure fronts and enhances local pressure superposition. The sequence (16-25-43) presents a more elliptical pressure distribution because paired wells located on opposite sides generate more directional pressure interference. Under full-well simultaneous energization (1~6), pressure fronts from all injection wells overlap within the same injection period, producing the strongest pressure superposition effect and the largest affected area; consequently, the average pore pressure reaches 40.3 MPa, which is 3.9 MPa higher than the best dual-well synchronized sequence and 6.2–6.4 MPa higher than the single-well sequential modes.



(a) The pore pressures with simultaneous energizing of injection wells (1~6) and sequential energizing of injection wells (1-2-4-6-5-3)



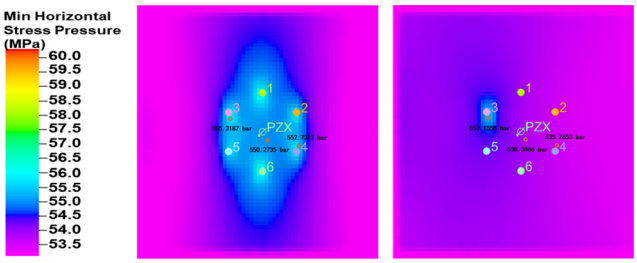
(b) The pore pressures with sequential energizing of injection wells (1-6-2-5-4-3) and sequential energizing of injection wells (16-25-43)



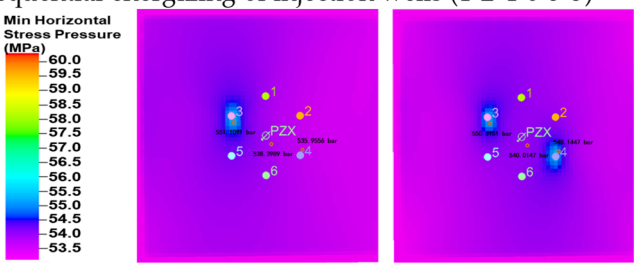
(c) The pore pressures with sequential energizing of injection wells (1-4-5-2-6-3) and sequential energizing of injection wells (12-46-53)

Figure 15. The pore pressure fields of the well group under different energy-storage sequences. (**a**) The pore pressures with simultaneous energizing of injection wells (1~6) and sequential energizing of injection wells (1-2-4-6-5-3); (**b**) The pore pressures with simultaneous energizing of injection wells (1-6-2-5-4-3) and sequential energizing of injection wells (16-25-43); (**c**) The pore pressures with simultaneous energizing of injection wells (1-4-5-2-6-3) and sequential energizing of injection wells (12-46-53).

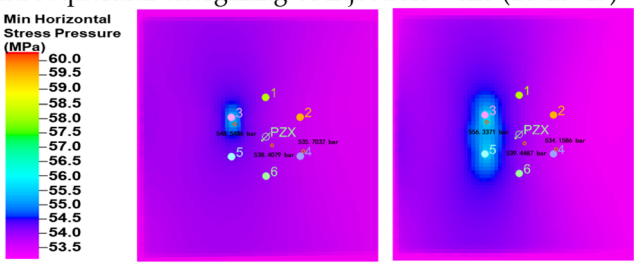
Building upon the preceding results, this study investigates the evolutionary patterns of the minimum horizontal principal stress field under varying energization sequences, using an inverted seven-spot well pattern model with a constant energy-storage injection rate, energy-storage volume, and constant-rate injection. As shown in Figure 16, the average maximum horizontal principal stresses of the well group under sequential energizing sequences (1-2-4-6-5-3), (1-6-2-5-4-3), (1-4-5-2-6-3), (16-25-43), and (12-46-53) were 54.1 MPa, 54.1 MPa, 54.1 MPa, 54.6 MPa, and 54.3 MPa. In contrast, with simultaneous energization of injection wells (1~6), the average minimum horizontal principal stress at equivalent monitoring positions reached 55.3 MPa.



(a) The minimum horizontal principal stresses with simultaneous energizing of injection wells (1~6) and sequential energizing of injection wells (1-2-4-6-5-3)



(b) The minimum horizontal principal stresses with sequential energizing of injection wells (1-6-2-5-4-3) and sequential energizing of injection wells (16-25-43)



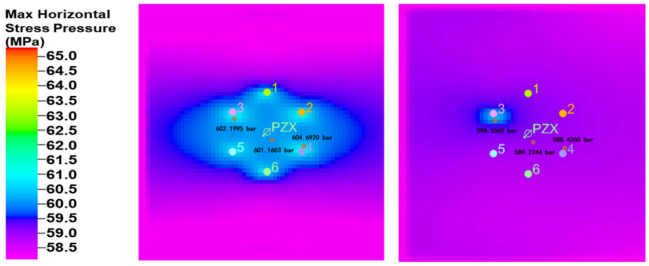
(c) The minimum horizontal principal stresses with sequential energizing of injection wells (1-4-5-2-6-3) and sequential energizing of injection wells (12-46-53)

Figure 16. The minimum horizontal principal stress fields of the well group under different energy-storage sequences. (**a**) The minimum horizontal principal stresses with simultaneous energizing of injection wells (1~6) and sequential energizing of injection wells (1-2-4-6-5-3); (**b**) The minimum horizontal principal stresses with simultaneous energizing of injection wells (1-6-2-5-4-3) and sequential energizing of injection wells (16-25-43); (**c**) The minimum horizontal principal stresses with simultaneous energizing of injection wells (1-4-5-2-6-3) and sequential energizing of injection wells (12-46-53).

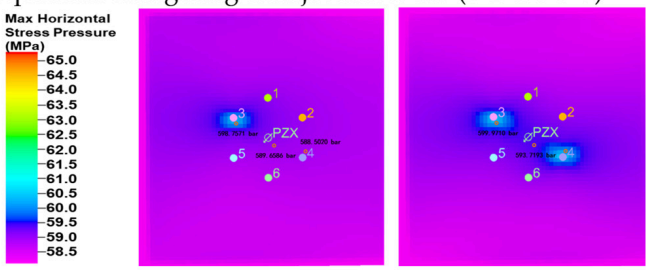
The analysis reveals significant variations in the influenced domains of the minimum horizontal principal stress field under different energization sequences. Under single-well sequential energization, the influenced domains are similar because stress perturbations generated by early-injected wells partially relax before subsequent wells are energized, leading to limited stress accumulation. Under dual-well synchronized sequential energization, the minimum horizontal principal stress increases moderately because two adjacent or opposite wells are pressurized at the same time, which enhances stress interference between paired injection wells. The average minimum horizontal principal stress reaches 54.6 MPa for sequence (16-25-43), higher than the single-well sequential modes. Under full-well simultaneous energization (1~6), the stress perturbations generated by all injection wells overlap in both time and space, producing the strongest stress-superposition effect. The average minimum horizontal principal stress reaches 55.3 MPa, which is 0.7 MPa higher than the best dual-well synchronized sequence and approximately 1.2 MPa higher than

the single-well sequential modes. These results demonstrate that the minimum horizontal principal stress response is controlled by both pressure-conduction timing and stress-field superposition.

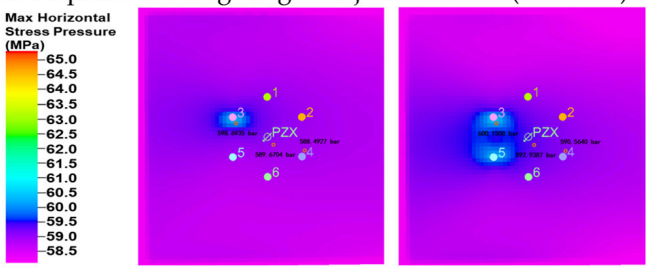
Similarly, this study systematically investigates the evolutionary patterns of the maximum horizontal principal stress field under varying energization sequences, revealing the operational control mechanisms governing stress field modulation. As shown in Figure 17, the average maximum horizontal principal stresses of the well group under sequential energizing sequences (1-2-4-6-5-3), (1-6-2-5-4-3), (1-4-5-2-6-3), (16-25-43), and (12-46-53) were 59.2 MPa, 59.3 MPa, 59.2 MPa, 59.7 MPa, and 59.4 MPa, respectively. In contrast, with simultaneous energization of injection wells (1~6), the average maximum horizontal principal stress at equivalent monitoring positions reached 60.3 MPa.



(a) The maximum horizontal principal stresses with simultaneous energizing of injection wells (1~6) and sequential energizing of injection wells (1-2-4-6-5-3)



(b) The maximum horizontal principal stresses with sequential energizing of injection wells (1-6-2-5-4-3) and sequential energizing of injection wells (16-25-43)



(c) The maximum horizontal principal stresses with sequential energizing of injection wells (1-4-5-2-6-3) and sequential energizing of injection wells (12-46-53)

Figure 17. The maximum horizontal principal stress fields of the well group under different energy-storage sequences. (**a**) The maximum horizontal principal stresses with simultaneous energizing of injection wells (1~6) and sequential energizing of injection wells (1-2-4-6-5-3); (**b**) The maximum horizontal principal stresses with simultaneous energizing of injection wells (1-6-2-5-4-3) and sequential energizing of injection wells (16-25-43); (**c**) The maximum horizontal principal stresses with simultaneous energizing of injection wells (1-4-5-2-6-3) and sequential energizing of injection wells (12-46-53).

The analysis reveals significant variations in the influenced domains of the maximum horizontal principal stress field under different energization sequences. Under single-well sequential energization, the average maximum horizontal principal stress varies only slightly among sequences (1-2-4-6-5-3), (1-6-2-5-4-3), and (1-4-5-2-6-3), with values of 59.2 MPa, 59.3 MPa, and 59.2 MPa, respectively. This small difference indicates that the long time interval between single-well injections weakens the cumulative stress response. Under dual-well synchronized sequential energization, the average maximum horizontal principal stress increases to 59.7 MPa for (16-25-43) and 59.4 MPa for (12-46-53). The improvement is attributed to the simultaneous pressure loading of paired wells, which enhances stress interference and expands the affected domain. Under full-well simultaneous energization (1~6), the highest average maximum horizontal principal stress of 60.3 MPa is observed at equivalent monitoring positions. This value is 0.6 MPa higher than the best dual-well synchronized sequence and 1.0–1.1 MPa higher than the single-well sequential modes. Therefore, compared with single-well sequential injection and dual-well synchronized injection, full-well simultaneous energization produces the strongest maximum horizontal stress superposition and the most continuous stress-affected zone within the inverted seven-spot well pattern.

3.4. Comparative Sensitivity of Energy-Storage Parameters

To clarify the priority of field parameter optimization, the sensitivities of injection rate, energy-storage volume, and injection sequence were compared horizontally based on the calculated response coefficients. For the pressure field, the injection rate shows the highest continuous-variable sensitivity, with an increase of 3.90 MPa per 1 m^3/min, followed by energy-storage volume, with an increase of approximately 0.79 MPa per 200 m^3. The injection sequence mainly affects pressure accumulation through temporal superposition: full-well simultaneous energization increases average pore pressure by 3.9 MPa compared with the best dual-well synchronized sequence and by more than 6.0 MPa compared with single-well sequential modes.

For the stress field, energy-storage volume has a stronger effect than injection rate on both minimum and maximum horizontal principal stresses when evaluated over the full tested range. Increasing the energy-storage volume from 2800 m^3 to 4200 m^3 increases the minimum and maximum horizontal principal stresses by 2.5 MPa and 2.6 MPa, respectively, whereas increasing the injection rate from 1.5 m3/min to 3.5 m3/min increases them by 1.4 MPa and 1.7 MPa, respectively. The injection sequence provides an additional stress-superposition gain, with the full-well simultaneous mode increasing the minimum and maximum horizontal principal stresses by 0.7 MPa and 0.6 MPa relative to the best dual-well synchronized sequence. Therefore, field optimization should prioritize the injection sequence for rapid well-group pressure build-up, then optimize the injection rate to improve pore-pressure response, and finally refine energy-storage volume according to cost, water-cut risk, and stress-control requirements.

4. Discussion

In summary, variations in the energy-storage injection rate, energy-storage volume, and energy-storage sequence significantly influence the coupled evolution of pore pressure–stress fields within the well group. In terms of injection-rate effects, high-rate energization induces a pressure-confinement effect within fractures, generating steep pressure-gradient fields that elevate intra-fracture fluid pressure. This hydraulic potential drives imbibition-dominated flow of the energization medium from fractures to matrix pores, thereby expanding the swept volume within the reservoir. The pressure-field sensitivity to injection rate reaches 3.90 MPa per 1 m^3/min, which is higher than the stress-field sensitivities

of 0.70–0.85 MPa per 1 m^3/min. Therefore, injection rate is a key parameter for rapid pore-pressure build-up. However, practical field operations require prudent optimization of the injection rate to mitigate operational risks associated with excessive rates, including fracture-network instability, pressure channeling, and unintended fluid migration.

It should be noted that the high coefficients of determination ($R^2 > 0.99$) reflect the monotonic responses obtained within the selected parameter ranges under a fixed geological model, grid configuration, and time-stepping strategy. They should not be interpreted as universal statistical relationships independent of model assumptions. The linearity is partly associated with the controlled single-factor simulation design, the prescribed range of injection rate and injected volume, and the deterministic representation of reservoir properties. Therefore, the regression results are mainly used to compare the relative sensitivity of engineering parameters rather than to provide field-scale probabilistic prediction.

The present simulation results are deterministic values, and confidence intervals were not calculated because sufficient stochastic realizations of porosity, permeability, and geomechanical parameters were not available. The geological model includes heterogeneity through the interpreted porosity and permeability distributions, but the coefficient of variation of these properties was not explicitly quantified in the available dataset. As a preliminary sensitivity assessment, this study focuses on three operational parameters: injection rate, energy-storage volume, and injection sequence. Future work should incorporate multiple geological realizations or Monte Carlo sampling of permeability, porosity, elastic modulus, and in-situ stress to quantify uncertainty envelopes for pore pressure and stress responses.

The pressure-confinement and imbibition-dominated flow mechanisms were further quantified using the simulated pressure increments and the 300 m well spacing. For example, increasing the injection rate from 1.5 to 3.5 m^3/min raises the average pore pressure by 7.8 MPa, corresponding to an apparent well-group pressure-gradient increment of approximately 0.026 MPa/m. Increasing the energy-storage volume from 2800 to 4200 m^3 produces a 5.5 MPa pressure increase, equivalent to approximately 0.018 MPa/m. Under different injection sequences, full-well synchronous energization produces a stronger pressure-front overlap than single-well sequential energization and dual-well synchronous energization, which explains its higher pore-pressure recovery and stronger stress superposition.

The internal mechanism can be interpreted from three aspects. First, increasing the injection rate strengthens the fracture-matrix pressure gradient and accelerates pressure propagation, so it has the most direct influence on rapid pore-pressure build-up. Second, increasing the injected volume extends the duration and spatial range of pore-fluid support, reduces the effective stress borne by the rock skeleton, and thus produces a stronger full-range stress response. Third, changing the injection sequence alters the temporal overlap of pressure fronts and stress perturbations among wells. Full-well simultaneous energization maximizes pressure-front overlap and stress-field superposition, whereas single-well sequential energization allows early pressure disturbances to dissipate before later injection starts. These mechanisms explain why the three engineering parameters show different sensitivities in the pore-pressure and stress-field responses.

Potential negative effects should also be considered during field implementation. Excessive injection rate or excessive energy-storage volume may increase the risk of uncontrolled fracture reorientation, excessive fracture-height growth, proppant migration or embedment, and leakage into neighboring layers. Consequently, although full-well synchronous energization is optimal for pressure recovery in the simulated cases, field application should combine pressure monitoring, fracture-height control, and stepwise injection optimization to avoid over-pressurization.

Recent studies on real-time monitoring systems in oil-processing equipment also emphasize that dense field measurements can improve diagnosis and model verification [27]. This further supports the need to combine numerical simulation with field pressure monitoring and production-dynamic feedback in future energy-storage fracturing design.

Regarding the impact of energy-storage volume on pore pressure–stress field evolution, the substantial injection of energization medium into the reservoir effectively replenishes the formation-energy deficit caused by prolonged production. Compared with lower energy-storage volumes, higher volumes enhance imbibition of fracturing fluid into matrix pores. This phenomenon arises from the dual pressure-bearing mechanism of reservoirs, in which stress is shared by the rock matrix and pore fluids. As the injected volume increases, the effective stress borne by the rock matrix decreases, whereas pore-fluid pressure rises, expanding the influenced domains of pore pressure–stress fields from localized near-well areas to the entire well network. The sensitivity comparison shows that energy-storage volume produces a stronger full-range increase in the horizontal principal stresses than injection rate, indicating that volume design is particularly important for stress-field adjustment and sustained energy replenishment. Nevertheless, excessive energy-storage volumes may increase flowback water cut and operating costs.

Regarding the influence of energy-storage sequences on pore pressure–stress field evolution, the differences among single-well sequential injection, dual-well synchronized injection, and full-well simultaneous injection are governed by two mechanisms: pressure-conduction time effects and stress-superposition effects. Single-well sequential injection has the longest time lag, so pressure from early-injected wells dissipates before later wells are energized, resulting in weak pressure accumulation. Dual-well synchronized injection shortens the time lag and strengthens local superposition between paired wells, improving both pressure and stress responses. Full-well simultaneous injection generates overlapping pressure fronts and synchronous stress perturbations across the entire well group, resulting in the highest average pore pressure and horizontal principal stresses. Therefore, injection sequence should be treated as the primary operational parameter for well-group synergistic energization, while injection rate and energy-storage volume should be jointly optimized according to pressure response, stress-control demand, and operational risk.

5. Conclusions

Through a comprehensive investigation of multi-field coupling evolution characteristics under group energy-storage fracturing in mature thin oil reservoirs, this study elucidates the influence of energy-storage injection rates, energy-storage volumes, and energy-storage sequences on pore pressure–stress fields. Key conclusions are summarized as follows:

(1) A statistically significant linear positive correlation exists between energy-storage injection rates and the coupled pore pressure–stress field evolution. When energy-storage injection rates were increased from 1.5 m^3/min to 3.5 m^3/min, the average pore pressure at equivalent monitoring positions rose by 7.8 MPa (20.69% enhancement), while the minimum and maximum horizontal principal stresses increased by 1.4 MPa (2.55%) and 1.7 MPa (2.83%), respectively. This trend was accompanied by a progressive expansion of the influenced domains for both pore pressure and stress fields, with propagation ranges transitioning from localized near-well regions to full well-network coverage.

(2) A statistically significant linear positive correlation is observed between energy-storage volumes and the coupled evolution of pore pressure–stress fields. Increasing the energy-storage volume from 2800 m^3 to 4200 m^3 elevates the average pore pressure at equivalent monitoring positions by 5.5 MPa (14.67% enhancement), while the

minimum and maximum horizontal principal stresses increase by 2.5 MPa (4.62%) and 2.6 MPa (4.41%), respectively. This volumetric dependency is accompanied by a progressive expansion of the influenced domains for both pore pressure and stress fields, with propagation ranges transitioning from localized near-well regions to full coverage of the inverted seven-spot well network.

(3) Energy-storage sequence significantly controls the coupled pore pressure–stress response of the well group. Among the tested schemes, simultaneous energization of injection wells (1–6) produced the strongest pressure-front overlap and stress-field superposition, yielding the highest average pore pressure of 40.3 MPa, minimum horizontal principal stress of 55.3 MPa, and maximum horizontal principal stress of 60.3 MPa at equivalent monitoring positions. Therefore, full-well simultaneous energization is the preferred operational mode for rapid well-group energy replenishment.

(4) The present work provides deterministic parameter-optimization results. The reliability of the regression relationships and the influence of reservoir heterogeneity should be further evaluated using field pressure data, production history matching, high-resolution monitoring-point data, and stochastic geological realizations.

Author Contributions: Methodology, Y.L.; Software, Z.X.; Validation, Z.L.; Formal analysis, Z.X.; Investigation, X.C. and Z.L.; Resources, X.C., Y.L. and X.T.; Writing—original draft, J.Z.; Writing—review & editing, J.Z.; Visualization, B.W.; Supervision, B.W.; Project administration, X.T.; Funding acquisition, X.C. and B.W. All authors have read and agreed to the published version of the manuscript.

Funding: This research was funded by financial support from the National Natural Science Foundation of China (No. 52374057) and the "Tianshan Talent" Training Program (2024TSYCCJ0010).

Data Availability Statement: Restrictions apply to the availability of these data. Data were obtained from PetroChina Xinjiang Oilfield Company and are available at https://www.cnpc.com.cn/cnpc/xjyt/sywq_column.shtml (accessed on 25 March 2026) with the permission of PetroChina Xinjiang Oilfield Company.

Conflicts of Interest: The authors Xiaolu Chen, Jianjun Zhang, Yingbiao Liu, Xiaochuan Tang, Zuxing Xiao and Zhenhu Lv were employed by the PetroChina Xinjiang Oilfield Company. The remaining author declares that the research was conducted in the absence of any commercial or financial relationships that could be construed as a potential conflict of interest. The PetroChina Xinjiang Oilfield Company had no role in the design of the study; in the collection, analyses, or interpretation of data; in the writing of the manuscript; or in the decision to publish the results.

References

1. Zou, C.N.; Yang, Z.; Zhu, R.K.; Zhang, G.S.; Hou, L.H.; Wu, S.T.; Tao, S.Z.; Yuan, X.J.; Dong, D.Z.; Wang, Y.M.; et al. Progress in China's Unconventional Oil & Gas Exploration and Development and Theoretical Technologies. *Acta Geol. Sin.* **2015**, *89*, 979–1007. [CrossRef]
2. Wang, R.Y.; Hu, Z.Q.; Dong, L.; Gao, B.; Sun, C.X.; Yang, T.; Wang, G.; Yin, S. Advancement and trends of shale gas reservoir characterization and evaluation. *Pet. Nat. Gas Geol.* **2021**, *42*, 54–65. [CrossRef]
3. Wang, Y.H.; Lu, Y.J.; Li, Y.P.; Wang, X.; Yan, X.M.; Zhang, Z.Y. Progress and application of hydraulic fracturing technology in unconventional reservoir. *Acta Pet. Sin.* **2012**, *33*, 149–158. [CrossRef]
4. Jiang, T.X.; Bian, X.B.; Sun, C.X.; Zhang, F.; Lin, L.; Wei, J.; Zhong, G. Key Technologies in Geology-Engineering Integration Volumetric Fracturing for Deep Shale Gas Wells. *Earth Sci.* **2023**, *48*, 1–13. [CrossRef]
5. Sheng, M.; Jiang, F.; Hu, S.; Lyu, Z.; Kong, M.; Si, L. The In-Situ Stress Interpretation in Heterogeneous Glutenite Reservoirs and Fracturing Design Optimization. *Xinjiang Oil Gas* **2024**, *20*, 1.
6. Li, H.T.; Luo, H.W.; Xiang, Y.X.; An, S.; Li, Y.; Jiang, B.; Xie, B.; Xin, Y. The Application Status and Prospect of DTS/DAS in Fracturing Monitoring of Horizontal Wells. *Xinjiang Oil Gas* **2021**, *17*, 62–73.
7. Xi, Z.Q.; Jia, S.P.; Wang, X.W.; Zhang, P.J.; Bi, Y.; Zhang, B. Analysis of the Pressure-Bearing Capacity of Carbonate Reservoirs for Gas Storage Based on Four-Dimensional Dynamic Geomechanics. *Xinjiang Oil Gas* **2024**, *20*, 63. [CrossRef]

8. Dai, X. Application of Massive Waterflooding Huff-Puff Technique in the Tight Oil Reservoir for Horizontal Wells. *Daqing Pet. Geol. Dev.* **2017**, *36*, 138–143. [CrossRef]
9. Yang, Y.D.; Yang, Z.Z.; Gan, Z.W.; Jiang, H.; Yi, Z.K. Application of Water-Flood Huff and Puff with Single Well in Tahe Oilfield. *Nat. Gas Explor. Dev.* **2006**, *29*, 32–35. [CrossRef]
10. Li, J.Q.; Yang, C.L.; Xu, C.E.; Ren, G.N.; Tu, X.W. Method of Improving Recovery Ratio for No Energy Complement Wells in South Yellow River Region. *Pet. Nat. Gas Geol.* **2001**, *22*, 221–224. [CrossRef]
11. Yang, F.; Li, Z.P.; Li, G. Study of Closed Time of Waterflood Stimulation in Carbonatite Reservoir. *Inn. Mong. Petrochem. Ind.* **2007**, *33*, 108–109. [CrossRef]
12. Zheng, T.Y.; Yang, Z.M.; Wang, Z.Y.; Dong, C.C.; He, Y. Carbon Dioxide Energy Storage Huff and Puff for Staged Fracturing Horizontal Wells in Tight Reservoirs. *Sci. Technol. Eng.* **2019**, *19*, 99–104. [CrossRef]
13. Huang, T.; Su, L.Y.; Da, Y.P.; Yang, A. Research and Field Test on Energy Storage Fracturing Mechanism of Horizontal Wells in Ultra-Low Permeability Reservoirs. *Pet. Drill. Tech.* **2020**, *48*, 80–84.
14. He, H.B. Practice of Re-Fracturing with Network Energization for Horizontal Well in Tight Oil Reservoir. *Unique Oil Gas Reserv.* **2018**, *25*, 170–174. [CrossRef]
15. Zhang, H.N.; Chen, J.T. Insights into Energy Storage Bulk Fracturing Technology for Low-permeability Oilfields—A Case Study of Peripheral Wellblock of Jilin Oilfield. *Unconv. Oil Gas* **2015**, *2*, 55–60.
16. Xiu, S.Z.; Jia, Y.Z.; Zhang, B.; Chen, S.Y.; Hao, Y.; Ge, T.Z. Research and Application of Height Control-Energizing-Network Fracturing Technology in Extremely-thick Low Permeability Glutenite Reservoirs. *Sino-Glob. Energy* **2016**, *21*, 58–63.
17. Hu, Z.W.; Han, Y.W. Feasibility study of energy storage using hydraulic fracturing in shale formations. *Appl. Energy* **2024**, *354*, 122251.
18. Li, K.K.; An, R.; Yue, P.D.; Chen, S.D.; Yang, K.L.; Wei, W. Large-scale energy storage volumetric fracturing technology for horizontal wells in the an 83 shale oil reservoir. *Pet. Drill. Tech.* **2021**, *49*, 125–129.
19. Zhou, H.; Yan, T.; Trivedi, J.; Wang, B.; Zhou, F. Investigating rock properties and fracture propagation pattern during supercritical CO_2 pre-fracturing in conglomerate reservoir. *Adv. Geo-Energy Res.* **2025**, *17*, 95–106. [CrossRef]
20. Zhou, H.; Yan, T.; Ma, C.; Wang, B.; Zhou, F. Characteristics of Propped Fracture Propagation in Volcanic Clastic Reservoirs: A Multiscale Study of Conductivity Sustainability and Fracture Network Complexity. *Rock. Mech. Rock. Eng.* **2025**, *58*, 12551–12576. [CrossRef]
21. Zhou, H.; Wang, B.; Zhou, F.J. Mechanical, structural, and mineralogical changes of shale under acid-CO_2-rock interactions and their implications for CO_2 storage. *Pet. Sci.* **2026**, *23*, 1261–1279.
22. Hu, Z.W.; Wang, H.Y.; Zheng, S. Numerical modelling of energy storage using hydraulic fracturing in shale formations. *Geoenergy Sci. Eng.* **2025**, *244*, 213424.
23. Sharp, J.M., Jr.; Simmons, C.T. The compleat Darcy: New lessons learned from the first English translation of Les Fontaines Publiques de la Ville de Dijon. *Groundwater* **2005**, *43*, 457–460. [CrossRef]
24. Coussy, O. *Poromechanics*; John Wiley & Sons: Hoboken, NJ, USA, 2004.
25. Biot, M.A. General theory of three-dimensional consolidation. *J. Appl. Phys.* **1941**, *12*, 155–164. [CrossRef]
26. Zienkiewicz, O.C.; Shiomi, T. Dynamic behaviour of saturated porous media; The generalized Biot formulation and its numerical solution. *Int. J. Numer. Anal. Methods Geomech.* **1984**, *8*, 71–96. [CrossRef]
27. Kukharova, T.; Martirosyan, A.; Asadulagi, M.-A.; Ilyushin, Y. Development of the Separation Column's Temperature Field Monitoring System. *Energies* **2024**, *17*, 5175. [CrossRef]

Disclaimer/Publisher's Note: The statements, opinions and data contained in all publications are solely those of the individual author(s) and contributor(s) and not of MDPI and/or the editor(s). MDPI and/or the editor(s) disclaim responsibility for any injury to people or property resulting from any ideas, methods, instructions or products referred to in the content.